AFRL-RI-RS-TR-2020-108

INVESTIGATING THE ROLE OF QUANTUM EFFECTS IN THE COMPUTATIONAL POWER OF OPTICAL COHERENT ISING MACHINES

THE UNIVERSITY OF TEXAS AT AUSTIN

JUNE 2020

FINAL TECHNICAL REPORT

APPROVED FOR PUBLIC RELEASE; DISTRIBUTION UNLIMITED

STINFO COPY

AIR FORCE RESEARCH LABORATORY
INFORMATION DIRECTORATE

■ **AIR FORCE MATERIEL COMMAND** ■ **UNITED STATES AIR FORCE** ■ **ROME, NY 13441**

NOTICE AND SIGNATURE PAGE

Using Government drawings, specifications, or other data included in this document for any purpose other than Government procurement does not in any way obligate the U.S. Government. The fact that the Government formulated or supplied the drawings, specifications, or other data does not license the holder or any other person or corporation; or convey any rights or permission to manufacture, use, or sell any patented invention that may relate to them.

This report is the result of contracted fundamental research deemed exempt from public affairs security and policy review in accordance with SAF/AQR memorandum dated 10 Dec 08 and AFRL/CA policy clarification memorandum dated 16 Jan 09. This report is available to the general public, including foreign nations. Copies may be obtained from the Defense Technical Information Center (DTIC) (http://www.dtic.mil).

AFRL-RI-RS-TR-2020-108 HAS BEEN REVIEWED AND IS APPROVED FOR PUBLICATION IN ACCORDANCE WITH ASSIGNED DISTRIBUTION STATEMENT.

FOR THE CHIEF ENGINEER:

/ S /
KRISTI MEZZANO
Work Unit Manager

/ S /
GREGORY HADYNSKI
Assistant Technical Advisor
Computing & Communications Division
Information Directorate

This report is published in the interest of scientific and technical information exchange, and its publication does not constitute the Government's approval or disapproval of its ideas or findings.

REPORT DOCUMENTATION PAGE

Form Approved
OMB No. 0704-0188

1. REPORT DATE *(DD-MM-YYYY)*	2. REPORT TYPE	3. DATES COVERED *(From - To)*
JUNE 2020	FINAL TECHNICAL REPORT	AUG 2018 – DEC 2019

4. TITLE AND SUBTITLE

INVESTIGATING THE ROLE OF QUANTUM EFFECTS IN THE COMPUTATIONAL POWER OF OPTICAL COHERENT ISING MACHINES

5a. CONTRACT NUMBER
N/A

5b. GRANT NUMBER
FA8750-18-1-0042

5c. PROGRAM ELEMENT NUMBER
62788F

6. AUTHOR(S)

Brian La Cour, Skylar Turner, Josey Hanish, and Noah Davis

5d. PROJECT NUMBER
CYDT

5e. TASK NUMBER
TX

5f. WORK UNIT NUMBER
AU

7. PERFORMING ORGANIZATION NAME(S) AND ADDRESS(ES)

The University of Texas at Austin
Research Laboratories
P.O. Box 8029
Austin, Texas 78713-8029

8. PERFORMING ORGANIZATION REPORT NUMBER

9. SPONSORING/MONITORING AGENCY NAME(S) AND ADDRESS(ES)

Air Force Research Laboratory/RITQ
525 Brooks Road
Rome NY 13441-4505

10. SPONSOR/MONITOR'S ACRONYM(S)
AFRL/RI

11. SPONSOR/MONITOR'S REPORT NUMBER
AFRL-RI-RS-TR-2020-108

12. DISTRIBUTION AVAILABILITY STATEMENT

Approved for Public Release; Distribution Unlimited. This report is the result of contracted fundamental research deemed exempt from public affairs security and policy review in accordance with SAF/AQR memorandum dated 10 Dec 08 and AFRL/CA policy clarification memorandum dated 16 Jan 09

13. SUPPLEMENTARY NOTES

14. ABSTRACT

The project investigates the role of quantum effects in the computational power of optical Coherent Ising Machines (CIM) and Measurement-Based Quantum Computing (MBQC). Both the CIM and photonic MBQC approaches share the critical feature of providing an alternative to the matter-based circuit model of quantum computation.

15. SUBJECT TERMS

Coherent Ising Machine, Quantum Computing, Quantum Error Correction

16. SECURITY CLASSIFICATION OF:			17. LIMITATION OF ABSTRACT	18. NUMBER OF PAGES	19a. NAME OF RESPONSIBLE PERSON
a. REPORT	b. ABSTRACT	c. THIS PAGE			**KRISTI MEZZANO**
U	U	U	UU	30	19b. TELEPHONE NUMBER (*Include area code*) **N/A**

Table of Contents

List of Figures

1 Summary

The original goal of this project was to study the coherent Ising machine (CIM) approach to solving quadratic binary optimization (QUBO) problems by considering the performance of a more fully quantum implementation. The CIM is a photonic annealer that uses optical parametric oscillators (OPOs) as surrogate

$$H(s_1,\ldots,s_n) = -\Big(\sum_i h_i s_i + \sum_{i<j} J_{ij} s_i s_j\Big)\,, \tag{1}$$

spins in a magnetic Ising model to solve hard optimization problems with a cost function of the form where $s_i = \pm 1$. The real-valued parameters (h_i) and (J_{ij}) define the given problem, and the values of $s_1,\ldots,s_n$ that minimize the cost function correspond to problem solutions.

Since the time of our original proposal, the field of optical computing had evolved rapidly. The CIM approach had been challenged by more recent improvements in classical computing methods and, overall, looked less promising than it did a year prior [4]. Nevertheless, there are a few out- standing questions regarding the efficacy of the CIM approach that we felt were worth pursuing. In particular, we wanted to see whether the incorporation of higher fidelity quantum modeling of the CIM, even if short of a full quantum representation, could mimic the qualitative behavior of the CIM and demonstrate a corresponding improvement in performance.

By contrast, the outlook for optical measurement-based quantum computing (MBQC) has looked quite promising. MBQC is a form of quantum computing that is particularly well suited to photonics and, unlike quantum annealing, is equivalent to the standard circuit (i.e., gate-based) model of quantum computing. In the MBQC model, we start

$$|\psi\rangle = \sum_{(i,j)\in\mathcal{G}} \mathbf{C}^{\mathbf{Z}}_{ij}\,|+\rangle_0 \cdots |+\rangle_{n-1}\,, \tag{2}$$

with an initial, highly entangled state of n qubits, called a "cluster state," which is the form where $\mathbf{C}^{\mathbf{Z}}_{ij}$ is the controlled $\mathbf{Z}$ gate between qubits i and j, $|+\rangle_k = [|0\rangle_k + |1\rangle_k]/\sqrt{2}$ is a superposition of binary states, and $\mathcal{G}$ is a graph defining the architecture of the cluster state. Gate operations are performed on $|\psi\rangle$ via local measurements.

Advances in silicon photonics have made a scalable implementation more feasible, yet there are still several open questions to explore [5]. Longer term, we believe this research direction will be more synergistic with the work in chip-based photonics at AFRL/RI and will lend to greater opportunities for collaboration between our two organizations in the future.

Both the CIM and photonic MBQC approaches share the critical feature of providing an alternative to the matter-based circuit model of quantum computation (e.g., ion

traps or superconducting circuits). The problems that need to be addressed in a photonic architecture are complementary to those in matter-based qubits; however, there are also fundamental differences that affect their potential relevance to the wider fields of quantum computation, communications, and sensing.

Exploring the open problems in a photonic MBQC is expected to lead to a better understanding to the role of errors and error correcting codes in quantum information processing. Procedures to generate large entangled cluster states have many applications beyond computation, e.g. quantum sensing and quantum networks, and this work was intended to improve the use of small quantum processors for the purification or transmission of quantum information between, say, nodes of a quantum network.

Because of the set of open and relatively unexplored problems, which are complementary to mainstream quantum computing approaches, as well as the likelihood that any results will have wide applicability beyond the confines of the larger goal of computing, we believed it would advantageous to reorient the main objectives of this proposal from an exploration of an optical CIM for quantum computation to an optical measurement-based implementation of quantum computation.

In light of these considerations, and based on feedback from the program officer for the project, ARL:UT proposed the following:

1. Use modeling and simulation to characterize the performance of an ideally implemented coherent Ising machine and compare this against current, state-of-the-art classical algorithms such as Simulated Annealing, Noisy Mean-Field Annealing, and Parallel Tempering.
2. Build high-fidelity simulations of realistic optical circuits based on current, state-of-the-art silicon photonics components for devices both commercially available and in development.
3. Use these simulation tools to characterize and model the stochastic noise and systematic bias of relevant computational circuits in the measurement-based quantum computing paradigm.

In the following sections, we will separate work on these two subtasks under the subsection headings CIM and MBQC for work on the Coherent Ising Machine and Measurement-Based Quantum Computing, respectively.

The work was led by the principal investigator, Dr. Brian La Cour, and co-investigator Dr. Antia Lamas-Linares. Technical development was led by Dr. Noah Davis, a post-doctoral fellow, and assisted by Skylar Turner, a physics graduate student, and Josey Hanish, and astronomy undergraduate student. In January 2019, Dr. Lamas-Linares left UT and was replaced by Dr. Lars Koesterke.

2 Introduction

2.1 CIM

In the CIM, the OPOs are discrete pulses in an optical fiber loop. Since the OPOs do not interact with each other, a small amount of signal is extracted via a beamsplitter, which is subjected to homodyne measurement and stored in a classical field-programmable gate array (FPGA). (See Fig. 1.) When combined with measurements from the other OPOs, a feedback signal is calculated classically in the FPGA and applied to each OPO in the next circulation. Over many loops around the annealer, the pump strength is increased from below the threshold for lasing. When the pump strength goes above this threshold, the spins bifurcate into up and down states.

As the FPGA is a classical device, this implementation of the CIM cannot truly be considered a quantum annealer, although it has been demonstrated to outperform other commercial quantum annealers such as those of D-Wave Systems [1]. (See Fig. 2.) As such, it is possible that classical algorithms and hardware may be able to match or beat the performance of the CIM in its current, FPGA-based implementation. In particular, King *et al.* have introduced a classical Noisy Mean Field Approximation (NMFA) algorithm that mimics the behavior of the CIM yet outperforms it on standard, classical hardware [2].

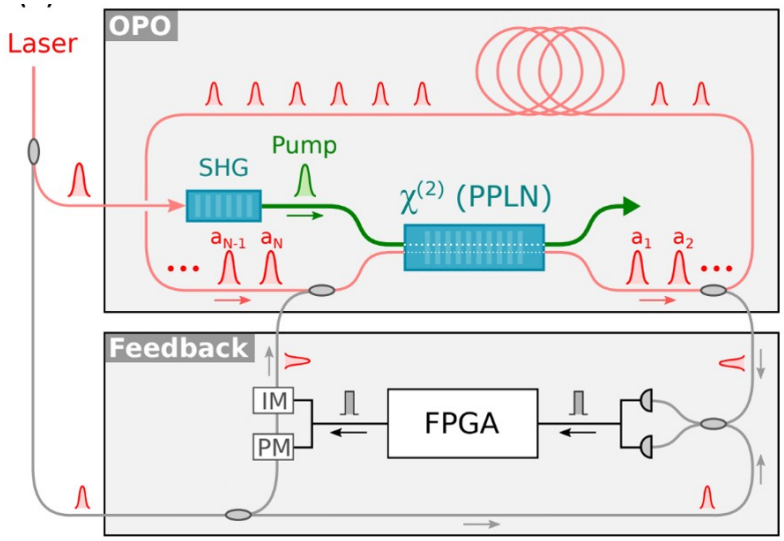

Figure 1: Schematical diagram of Coherent Ising Machine. (From Ref. [1].)

2.2 MBQC

Photonic MBQC devices are distinct, and in many ways complementary, to those in material qubit systems. Photons do not suffer the same susceptibility to environmental noise and decoherence as do material qubits [6]. On the other hand, manufacturing defects in photonic chips can lead to pervasive systematic biases in gate operations and measurements. However, since these biases persist even for classical light, it is relatively easy to calibrate and account for them [7]. This conveniently allows one to handle errors at the software level by defining physical gates to correct for known systematic errors.

The main challenge in photonic MBQC systems is the lack of on-demand single-photon sources and perfect photon detectors. We have found that the former may be approximated using a network of delayed photon heralding for which a single photon can be guaranteed with near certainty but only after a fixed time τ. Using a bank of n entangled photon pairs, each signal photon is delayed by a time τi and is paired with an idler photon that heralds at a time $\tau - \tau i$. (Subsequent heralded photon detections are then ignored.)

2.2.1 Generation of cluster states

To create the cluster states needed for photonic MBQC gate operations, a series of "fusion gates" are needed to create every more entangled states from parametric downconversion (PDC) sources that provide the initial entangled pairs. Type I fusion gates allow one to create arbitrarily large linear cluster states, which may be used for performing single-qubit gate operations, but Type II fusion gates are required to create the 2D cluster states needed for general two-qubit operations [3]. Ignoring detection efficiencies, both Type I and Type II fusion gates have a 50% probability of success owing to the partial collapse of the quantum state during the measurement process. The use of "boosted" fusion gates can increase this probability to 75% [8].

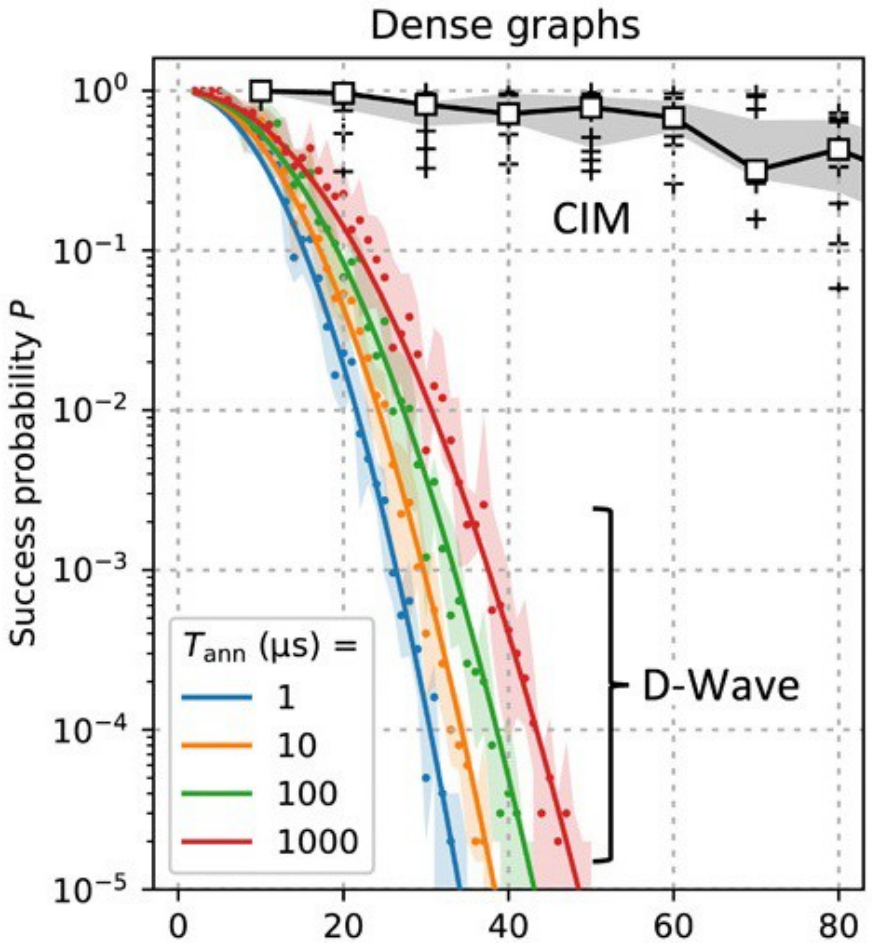

Figure 2: Comparison of the CIM versus the D-Wave machine. (From Ref. [1].)

The operation of a Type I fusion gate is illustrated in Fig. 4. Two sources of entangled photon pairs generated through spontaneous parametric downconversion (PDC) are required. A photon from each pair is used to perform a single local measurement in the **X** (i.e., D/A) basis using a half- wave plate (HWP) to perform a Hadamard transformation (**H**), followed by a polarizing beamsplitter (PBS) to measure in the **Z** (i.e., H/V) basis.

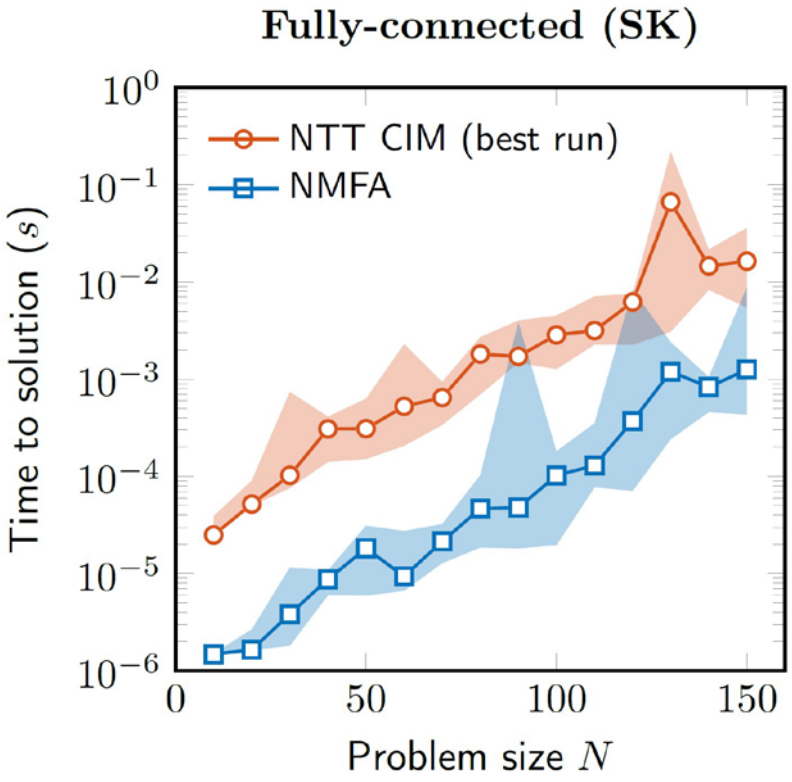

Figure 3: Comparison of the CIM versus the NMFA algorithm. (From Ref. [2].)

Suppose the first PDC produces photon pairs in the state

$$|\psi\rangle_{12} = \frac{1}{\sqrt{2}}\left(|HH\rangle_{12} + |VV\rangle_{12}\right), \tag{3}$$

as illustrated in Fig. 4. Equivalently, this may be written in the Heinsenberg picture as an operator on the vacuum state and of the form

$$\hat{\mathbf{A}}_{12} = \frac{1}{\sqrt{2}}\left(\hat{a}_1^\dagger \hat{a}_2^\dagger + \hat{b}_1^\dagger \hat{b}_2^\dagger\right), \tag{4}$$

where $\hat{a}_i^\dagger$ and $\hat{b}_i^\dagger$ are the creation operators for the horizontal and vertical polarization modes, respectively, of photon i. A similar expression applies for photons 3 and 4.

Passage of photons 2 and 3 into the initial PBS and HWP result in the following state:

$$\frac{1}{2}\hat{a}_1^\dagger \hat{a}_2^\dagger \hat{b}_2^\dagger \hat{b}_4^\dagger + \frac{1}{2}\left(\frac{\hat{a}_1^\dagger \hat{a}_2^\dagger \hat{a}_4^\dagger + \hat{b}_1^\dagger \hat{b}_2^\dagger \hat{b}_4^\dagger}{\sqrt{2}}\right)\hat{a}_3^\dagger + \frac{1}{2}\left(\frac{\hat{a}_1^\dagger \hat{a}_2^\dagger \hat{a}_4^\dagger - \hat{b}_1^\dagger \hat{b}_2^\dagger \hat{b}_4^\dagger}{\sqrt{2}}\right)\hat{b}_3^\dagger + \frac{1}{4}\hat{b}_1^\dagger \hat{a}_4^\dagger\left[(\hat{a}_3^\dagger)^2 + (\hat{b}_3^\dagger)^2\right] . \tag{5}$$

Measurement is performed on spatial mode 3 (i.e., $\hat{a}_3^\dagger$ and $\hat{b}_3^\dagger$). With probability ¼, no photons are detected, and the procedure fails (first term). With probability ¼ a single H photon is detected and the state collapses to a standard GHZ state (second term), which is the desired outcome. With probability ¼, a single V photon is detected and the state collapses to a nonstandard GHZ state (third). In this case, local operations may be performed to transform it into standard form. For example, we may apply a single-phase gate **Z** to anyone (or all) of photons 1, 2, and 4. Finally, with probability, we will measure either two H photons or two V photons. Determining this requires photon number resolving (PNR) detectors or the use of pairs of single-photon detectors with 50/50 beamsplitters. In this case, the procedure fails.

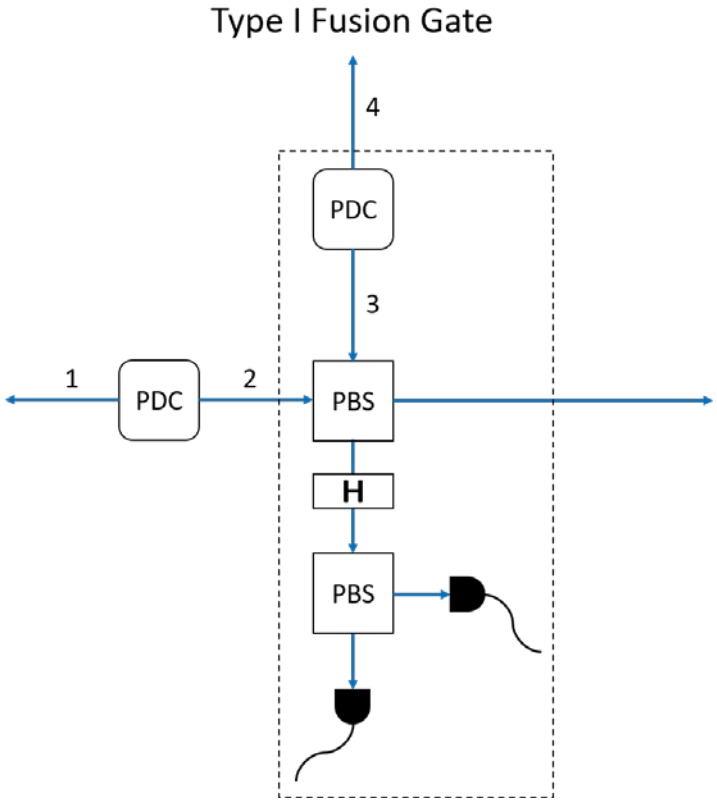

Figure 4: Type I fusion gate, as indicated by the dashed box. (Adapted from Ref. [3].)

Ignoring detector inefficiencies, and assuming a set of Bell pairs has indeed been prepared, the whole process works successfully half of the time. Type I fusion gates may be chained to form arbitrarily long linear chains of entangled states. The notional architecture is sketched in Fig. 5. If *R* is the rate of entangled pair production from a single PDC, then the rate of simultaneous pair production for *n*

Type I fusion gates is R^{n+1}, since there is one PDC per fusion gate. Furthermore, each gate has a ½ probability of success, given the presence of two entangles pairs, so the rate of success for producing linear chains of n+2 photons is $R(R/2)^n$.

Linear chains are sufficient to perform single-qubit operations via MBQC, which by itself is not useful. To perform two-qubit operations, which are needed for universal computing, a cluster state of at least two dimensions is needed. For this purpose, a Type II fusion gate may be used. The basic operation is illustrated in Fig. 6. A photon from each of two entangled pairs is put into the gate and measured, sacrificing both. The photons enter into a D/A PBS, illustrated here as a standard H/V PBS with half-wave plates at each port. The two output ports are subjected to a standard four-mode measurement. The final state, before measurement of spatial modes 2 and 3, is

$$\frac{1}{2}\hat{c}_1^\dagger \hat{d}_4^\dagger\left[(\hat{a}_2^\dagger)^2-(\hat{b}_2^\dagger)^2\right]+\frac{1}{2}\hat{d}_1^\dagger \hat{c}_4^\dagger\left[(\hat{a}_3^\dagger)^2-(\hat{b}_3^\dagger)^2\right] + \frac{1}{2}\left(\hat{c}_1^\dagger \hat{c}_4^\dagger+\hat{d}_1^\dagger \hat{d}_4^\dagger\right)\left(\hat{a}_2^\dagger \hat{a}_3^\dagger+\hat{b}_2^\dagger \hat{b}_3^\dagger\right)+\frac{1}{2}\left(\hat{c}_1^\dagger \hat{c}_4^\dagger-\hat{d}_1^\dagger \hat{d}_4^\dagger\right)\left(\hat{a}_2^\dagger \hat{b}_3^\dagger+\hat{b}_2^\dagger \hat{a}_3^\dagger\right). \quad (6)$$

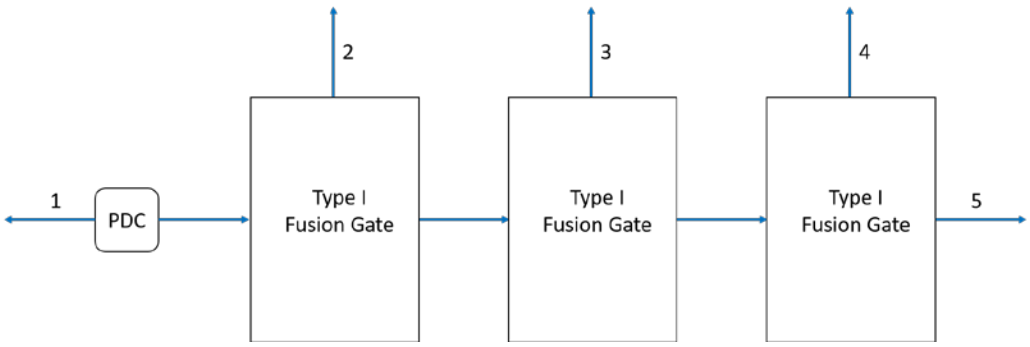

Figure 5: Type I fusion gate chain forming a linear cluster state.

The first two terms correspond to a detection in exactly one of the four spatial modes, which is rejected as a failure and occurs 50% of the time. The remaining two terms correspond to detections in exactly two modes, corresponding to a success. The collapsed state is a maximally entangled Bell state between photons 1 and 4.

Although creating one entangled pair from two entangled pairs in unremarkable, the spatial modes 1 and 4 could themselves represent larger entangled states, such as linear cluster states created from Type I fusion gates. In this way, one may use Type II fusion gates to entangle and "stitch together" other entangled states to create an arbitrarily larger cluster state. Using a combination of Type I and Type II fusion gates therefore allows one to create an arbitrarily large cluster state suitable for universal MBQC.

2.2.2 Quantum error correction for MBQC

We investigated quantum error correction on the 3D color code with boundaries, also known as the "tetrahedral color code," which is a necessary structure for "colorful quantum computing" [9]. We developed an algorithm for decoding **X** and **Z** errors on the tetrahedral color code. This algorithm was adapted from the "restriction decoder," an algorithm for decoding color codes with periodic boundaries [10]. We characterized the performance of this decoder on independent, identically distributed **X** and **Z** errors and determined thresholds for error-correction such that for noise below the threshold, the probability of logical errors can be made arbitrarily small by using larger size codes. These results form a significant contribution to colorful quantum computing and other recent proposals for fault-tolerant quantum computing in photonic MBQC. In this effort we were aided by Mr. Eion Blanchard, a visiting scholar and graduate student in mathematics from the University of Illinois at Urbana-Champaign whose work was partially funded under this grant.

Colorful quantum computing uses a 3D color code that can be implemented on a 2D lattice of physical qubits using "just-in-time decoding." This scheme achieves universality with only transversal gates, circumventing the Eastin-Knill Theorem [11] by relying on non-local classical computing [9]. Transversal gates, which operate "qubit-wise" on physical qubits, are highly desirable for fault-tolerant codes because they propagate errors only locally [12]. Colorful quantum computing is fault-tolerant, though the noise threshold for fault-tolerance has only been investigated theoretically [9] and is very low. However, thresholds found using direct simulation of the error-correction process are usually much higher.

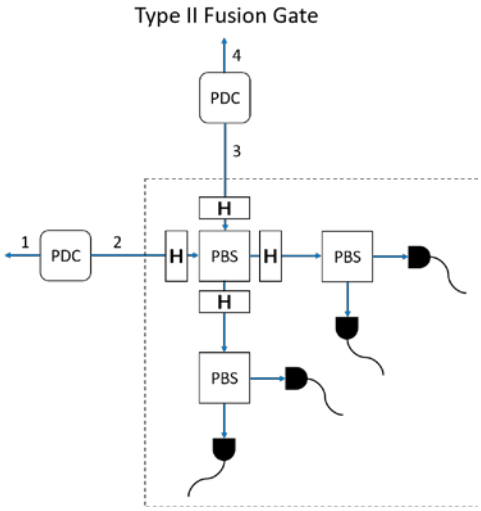

Figure 6: Type II fusion gate. (Adapted from Ref. [3].)

The tetrahedral color code admits the following transversal logical gates [12]: The logical Controlled- $\mathbf{X}$ (CNOT) gate can be applied by applying CNOT pairwise between corresponding physical qubits of two logical qubits. The Controlled-$\mathbf{Z}$ ($c\mathbf{Z}$) gate is applied analogously, but by matching qubits on only one facet of a primal tetrahedron to qubits on one facet of another primal tetrahedron. Most importantly, the $\mathbf{T}$ gate is transversal. The logical $\mathbf{T}$ gate is applied by applying $\mathbf{T}$ to a set of the physical qubits and $\mathbf{T}^\dagger$ to the remainder, such that the two sets are a bipartition of the lattice. The logical $\mathbf{T}^2$ gate is also transversal, as are the logical $\mathbf{X}$ and $\mathbf{Z}$.

When supplemented with measurements in the $\mathbf{Z}$ basis $\{|0\rangle, |1\rangle\}$, $\mathbf{X}$ basis $\{|\pm\rangle = |0\rangle \pm |1\rangle$, and $\mathbf{X} + \mathbf{Y}$ basis $\{|0\rangle \pm e^{i\pi/4}|1\rangle\}$, this set of gates for the tetrahedral color code becomes universal in measurement-based quantum computing (MBQC). An example of how to implement the Hadamard gate in such a scheme can be found in Refs. [13, 9]. MBQC is equivalent to the circuit model, but implemented differently - all entanglement is present in a resource state at the beginning of the computation. Gates are simulated by qubit measurements on a highly entangled *cluster state*, and a classical computer processes the Pauli frame [14]. Universality requires a cluster state of at least two dimensions and the ability to measure qubits in the $\mathbf{X}$, $\mathbf{Z}$, and $\mathbf{X} + \mathbf{Y}$ bases. Generating a cluster state requires a source of $|+\rangle$ states and the ability to apply the $c\mathbf{Z}$ gate between neighboring qubits [15].

Colorful quantum computing is a type of MBQC that encodes the logical qubits of the cluster state in a tetrahedral color code. Arranged in this way, the initial state forms a 3D lattice of qubits. The cluster state is initialized using $c\mathbf{Z}$ gates, $|+\rangle$ states, and ancilla qubits. Afterwards, the logical qubits form a cluster state up to known single-qubit Pauli errors, i.e. the Pauli frame. An $\mathbf{X}$ decoder is used to determine the Pauli frame and the locations of errors are stored in a classical memory. The measurement pattern is then enacted by measuring the logical qubits in the appropriate basis, which requires either an X decoder, a $\mathbf{Z}$ decoder, or both. If the logical measurement is in the $\mathbf{X} + \mathbf{Y}$ basis, a transversal $\mathbf{T}$ gate is applied before measuring in the $\mathbf{X}$ basis, which requires a $\mathbf{Z}$ decoder to interpret. This scheme does not require magic state distillation because the $c\mathbf{Z}$ and $\mathbf{T}$ gates are transversal, as are measurements in the Pauli bases. The ability of colorful quantum computing to realize fault-tolerant, universal quantum computing without magic state distillation motivates our development of decoders for the color code with boundaries.

3D color codes are a type of error-correcting stabilizer code. In the stabilizer formalism, states are described not by a wavefunction but by stabilizer operators. The state described by a set of stabilizer operators $\mathbf{S}$ is the +1 eigenstate of each operator, $\mathbf{S}\ |\psi\rangle = |\psi\rangle$, $\mathbf{S} \in \mathcal{S}$. An n-qubit state described by k independent, commuting stabilizers inhabits a 2^{n-k} dimensional subspace. Operators that commute with the set of stabilizers are denoted $\mathcal{Z}$, and non-trivial logical operators are $\mathcal{Z} \setminus \mathcal{S}$. In the context of stabilizer codes, the code space is the 2^{n-k} dimensional +1 eigenstate of the code stabilizers. To define a basis for the $n - k$

logical qubits, one chooses $n-k$ logical $\bar{Z}_i$ operators $\bar{Z}_i$ from $\mathcal{Z} \setminus \mathcal{S}$. Then one can choose logical $\bar{X}_i$ operators such that $\bar{X}_i \bar{Z}_j = (-1)^{\delta_{ij}} \bar{Z}_j \bar{X}_i$

An error, $\mathbf{E}$, will anticommute with at least one stabilizer if the error is *correctable*. This results in a -1 measurement outcome when one of those stabilizers is measured. Thus, we measure a generating set of stabilizers to find the *syndrome* corresponding to the error $\mathbf{E}$, which we then decode to obtain the corresponding *correction operator*, τ. Finally, we apply this correction operator to bring the system back into the code space. Error correction fails when the combination of errors and correction operators is a logical operator; i.e., $\tau \mathbf{E} \notin \mathcal{Z} \setminus \mathcal{S}$.

3 Methods, Assumptions, and Procedures

3.1 CIM

We began our investigations by considering several classical benchmark problems. Classical algorithms have been shown to outperform the CIM in terms of both success probability and time-to- solution metrics [2, 16]. Of these, the fully classical Noisy Mean Field Annealing (NMFA) algorithm is notable because it emulates the OPO feedback scheme used by the CIM. Like the CIM, the NMFA algorithm measures the spins, computes interaction terms, and then uses these terms to provide feedback to evolve the spins further. We used the NMFA algorithm as a classical benchmark due to this similarity.

We implemented the NMFA algorithm and compared the success probabilities to benchmarked solutions obtained through brute force classical search algorithms. For this purpose, a suite of QUBO problems were considered, including antiferromagnetic rings, Mobius ladders, Sherrington- Kirkpatrick spin glass, and dense Max-Cut problems. Exact global ground state solutions were found through direct computation or using the Spin Glass Server from the University of Cologne [17]. We found that NMFA has a nearly perfect success probability for problems with less than 50 spins and a good success probability (between 0.01 and 0.2) for problems with 50 to 100 spins, exhibiting an exponential fall off in with increasing spin number.

We next considered CIM performance against classical algorithms by analyzing a more fully quantum mechanical modeling approach. The CIM may be described by a master equation for the density operator $\hat{\rho}$ describing the number states for the pump and each OPO. Mathematically, this takes the form of a multidimensional coupled stochastic differential equation for the components of the corresponding operators in matrix form. The stochasticity of the description arises from the phenomenological modeling of the homodyne measurement process, which is assumed to introduce noise through a Brownian motion process. Other physical effects represented in the master equation include pump-OPO photon exchange, OPO feedback, and interactions of the fields with the nonlinear crystal.

We considered two approximations of the master equation. The first, the stochastic approximation, describes the solution in terms of a two-parameter positive P basis, wherein

$$\hat{\rho} = \int\int \hat{\Lambda}(\alpha,\beta)\, P(\alpha,\beta)\, d\alpha\, d\beta\,, \tag{7}$$

where $\hat{\Lambda}(\alpha,\beta)$ is a projection onto the coherent states $|\alpha\rangle$, $|\beta\rangle$, and $P(\alpha,\beta) \geq 0$ is a (true) probability density. Writing the master equation in the positive P basis, we obtain a coupled stochastic differential equation for the coefficients α_i, β_i corresponding to each OPO. (The pump is treated classically as depletion free and, hence, is a fixed parameter.)

The probability density function arising from the positive P representation is, in general, non-Gaussian. Approximating it to be Gaussian by considering only the first and second moments leads to the second approximation of the master equation we considered, the Gaussian approximation. Here, the system is described by a coupled system of stochastic differential equations for the mean μ_i and variance σ_i^2 of each OPO. (In this approximation, there are no correlations between OPOs.)

3.2 MBQC

3.2.1 Structure of the color code

3D color codes are topological stabilizer codes. These codes are defined on lattices in which stabilizers correspond to topological objects, such as loops or surfaces. An accessible introduction to color codes (of all dimensions) may be found in Ref. [18]. Here, we investigate *tetrahedral* color codes, which are 3D color codes with non-periodic boundary conditions [19].

We define the tetrahedral color code on a dual lattice $\mathcal{L}^*$ such that tetrahedra [3-simplices, denoted $\Delta 3(\mathcal{L}^*)$] specify the physical qubits, vertices [0-simplices, $\Delta 0(\mathcal{L}^*)$] generate the set of **X** stabilizers and edges [1-simplices, denoted $\Delta 1(\mathcal{L}^*)$] generate the set of **Z** stabilizers. The tetrahedral color code depicted in Fig. 7 has 15 qubits, four **X** stabilizers, and 18 **Z** stabilizers.

Each vertex of $\mathcal{L}^*$ is assigned a color from the set $\mathcal{C} = \{r, g, b, y\}$ such that no adjacent vertices share a color. Each edge is labeled by the two colors that are absent from the vertices it connects. For example, a by-colored edge connects an r-colored vertex and a g-colored vertex.

We refer to the four boundary vertices of the code as quasivertices. The quasivertices do not correspond to **X** stabilizers, and the tetrahedron formed by connecting all the quasivertices does not correspond to a physical qubit. However, the edges and tetrahedra adjacent to the quasivertices are **Z** stabilizers and physical qubits,

respectively.

For the purposes of physical implementation, it is simpler to define the tetrahedral color code differently. Before, we used the dual lattice description $\mathcal{L}^*$, and now we introduce the primal lattice description $\mathcal{L}$. In the primal lattice, qubits are vertices, **Z** stabilizers correspond to faces, and **X** stabilizers are cells. The four boundaries now appear as triangular facets.

In the simplest possible primal lattice, shown in Fig. 7, each face is adjacent to four qubits and each cell is adjacent to eight qubits. It is harder to see, but in the corresponding dual lattice each edge and vertex is adjacent to four or eight tetrahedra, respectively. We analyze a family of codes built in the dual on the body-centered cubic, or *bcc*, lattice. In the corresponding primal lattice each cell in the bulk is a bitruncated cube.

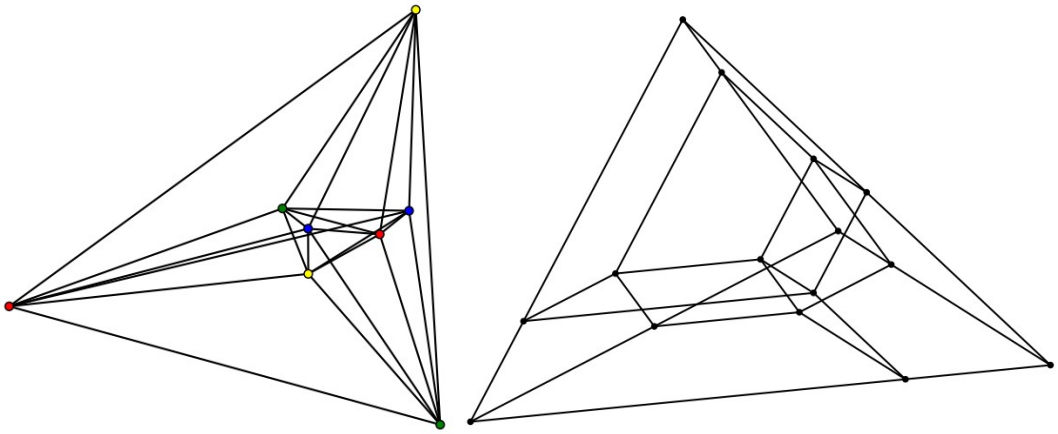

Figure 7: A representation of the smallest tetrahedral color code, in the dual (left) and primal (right) lattice.

Every tetrahedral color code encodes a single logical qubit in a larger number of physical, or code, qubits. A common basis for a single logical qubit is one in which the logical operators $\bar{\mathbf{X}}$ and $\bar{\mathbf{Z}}$ are tensor products of **X** and **Z** operators, respectively, on each of the physical qubits.

3.2.2 X errors — loop-like syndromes

We implement the cellular automaton-based restriction decoder described in [10], adapting it to a lattice with a tetrahedral boundary (as opposed to a lattice with periodic boundaries). The syndrome of an **X** error appears as a collection of edges that bound the set of tetrahedra corresponding to the qubits that have errors. Given a set of edges $\sigma \subset \Delta 1(\mathcal{L}^*)$, we find the set of tetrahedra $\tau \subset \Delta 3(\mathcal{L}^*)$ such that $\sigma = \partial 3,1(\tau)$, where $\partial n,m$ denotes the projection of an n-dimensional set of objects to its m-dimensional boundary.

The restriction decoder achieves this via two routines: the "sweep decoder and the "lift routine. One of the four lattice colors is chosen as the lift color; the rest are sweep colors. For each sweep color, the decoder considers the subset of edges in σ labeled with the particular sweep color (i.e. only syndrome edges not incident to a sweep-colored vertex are considered). The decoder then runs the sweep decoder [20], a toric-code decoder, on this subset of edges to obtain a set of faces whose boundary is the set of edges having been considered. The faces resulting from each sweep color are taken in union as $\gamma \subset \Delta 2(\mathcal{L}^*)$. Then $\partial 2,1(\gamma) = \sigma$.

Next, considering the subset of vertices assigned the lift color, the decoder identifies the set of tetrahedra $\gamma \subset \Delta 3(\mathcal{L}^*)$ such that $\partial 3,2(\gamma) \subset \gamma$ and for each lift vertex v, $\partial 3,2(\gamma)|_v = \gamma|_v$, where $\gamma|_v$ is the subset of γ containing v. We note the naïve treatment of boundary vertices in the lift process. Lifting each bulk (interior) vertex runs in constant time since there are 2^{12} possible subsets of tetrahedra incident to each bulk vertex (a consequence of the lattice geometry). With non-periodic boundaries as in our code lattice, however, the tetrahedral neighborhoods of boundary vertices become increasingly dense at a quadratic asymptotic rate $O(d^2)$, where d is the code distance. So, our naïve approach runs in at-worst exponential time: $O(2^{d^2})$

To overcome this computational hurdle, we adapt the "peel" algorithm described in [21] to lift boundary vertices more efficiently. (See Fig. 8.) In fact, on code lattices with small distance, this is more efficient than the naïve lift on even the bulk vertices. The peel algorithm proceeds on each lift vertex v by taking the set of tetrahedra $\tau|_v$ incident to v and considering $\partial 3,2(\tau|_v) \setminus (\partial 3,2(\tau|_v) |_v)$. That is, we consider the set of faces which are incident to $\tau|_v$ but disjoint from v itself (i.e. faces whose vertices are in the *link* of v); these faces form a topological sphere when v is a bulk vertex and form a triangular facet when v is a boundary vertex.

We consider the subset of "intermediate syndrome" faces which is output from the sweep decoder) that are incident to v: $\gamma|_v$ (brown faces in Fig. 8a). We project this set of faces $\gamma|_v$ into a set of edges (purple in Fig. 8b) on the aforementioned "peeling surface" (topological sphere or tetrahedral facet). The peel algorithm finishes by identifying the set of faces (Fig. 8c) on the surface whose edge-boundary matches these projected edges, which can be done efficiently following Ref. [21], then projects the triangle faces back up to tetrahedra, with the associated lift vertex v as the fourth vertex for each tetrahedra. The resulting set of tetrahedra from all lift vertices is the desired τ.

The peel subroutine runs in asymptotically constant time for bulk vertices. Its runtime on boundary vertices is now $O(d^2)$, a vast improvement over the original lift procedure. In addition, decoding is done locally.

3.2.3 Z errors — point-like syndromes

The syndrome of **Z** errors is a set of vertices corresponding to **X** stabilizers that returned a -1 measurement outcome. We use a minimum-weight perfect matching (MWPM) subroutine to find edges that connect these vertices. First, we restrict the dual lattice to include only vertices of two colors; that is, for C as above, vertices assigned color κi or κj are removed, while vertices assigned κk or κl remain (for $\kappa i \neq \kappa j \neq \kappa k \neq \kappa l$). We then match the syndrome vertices on each twice-restricted lattice and take the union of all returned sets of edges. Those edges correspond to the syndrome that would occur if **X** errors had occurred on the qubits actually affected by **Z** errors. Finally, the **X** error decoder, described above, is called as a subroutine to identify the error qubits. This is the approach used in [22], which can be thought of as a specific implementation of the more general process described by the restriction decoder [10].

To handle the boundary, we adapt the MWPM algorithm to allow for vertices to match to the nearest quasivertex that remains in the twice-restricted lattice. We add edges between each vertex and its nearest quasivertex, which can be either color. In addition, we add weight-0 edges between quasivertices so that the solutions that do not include a quasivertex-vertex edge are matchings. This is the same process that is used to decode the surface code using MWPM [23], and it is not computationally any more difficult than decoding without boundaries. Our decoding scheme corrects the smallest set of error qubits that could have caused the given syndrome. This is a justified choice since the probability p^n of an n-qubit error decreases as n increases; smaller errors are more likely. Because of this, the decoder tends to match bulk vertices to the boundary quasivertices, while an observer who knows the positions of the original error qubits would expect that vertex to be matched to a bulk vertex. This limits succesful error-correction of **Z** errors, as the smallest-weight logical errors of tetrahedral color codes are **Z** errors on the d qubits that connect two quasivertices by the edges between two facets. It may be possible to weight edges that connect quasivertices to bulk vertices to avoid this situation, like the flag qubit scheme used in Ref. [24]. We leave more sophisticated ways to handle Z boundary errors for future research.

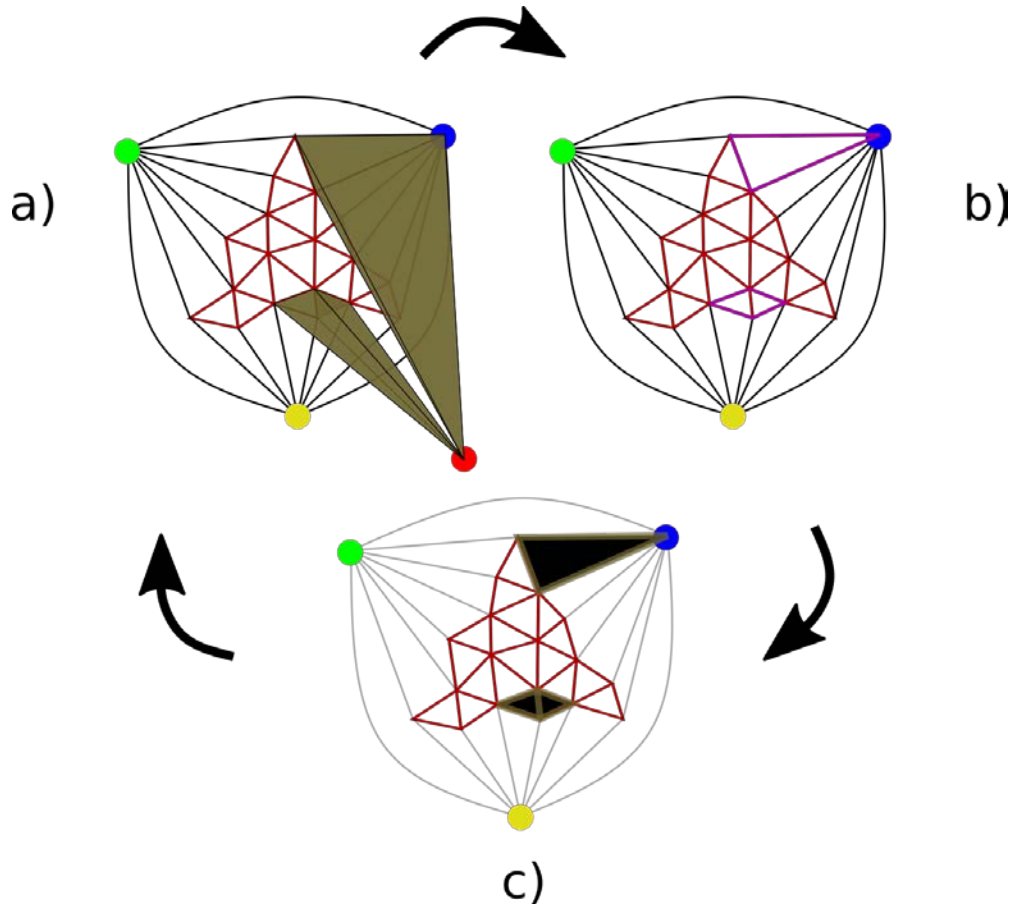

Figure 8: Illustration of the efficient lift procedure on a boundary quasivertex. In a), lift must find which tetrahedra in the neighborhood of the red quasivertex have a boundary of faces that match the brown highlighted ones. b) We project the marked faces onto the facet nearest the red quasivertex, marking a purple edge for each face's intersection with the facet. c) On the facet, it is possible to quickly find the 2D boundary of these edges marked in black. These faces have a one-to-one correspondence with the error qubits adjacent to the red quasivertex.

The **Z**-error decoder is necessarily less successful than the **X**-error decoder: there are fewer **X** stabilizers than there are **Z** stabilizers, and **X** stabilizers have higher weight than **Z** stabilizers, so **Z**-error syndromes contain less information than **X**-error syndromes. The **Z**-error decoder also has a worse runtime than the **X**-error decoder because of the repeated MWPM subroutines.

4 Results and Discussion

4.1 CIM

We performed numerical simulations of the CIM time evolution under both the stochastic and Gaussian approximations using the benchmark problems developed over the previous quarter and compared their performance to that of the NMFA algorithm. In general, the stochastic approximation outperformed the Gaussian approximation, suggesting that a more fully quantum approach does yield better performance. However, the classical NMFA algorithm outperformed both of these. This result showed promise for a full master equation solution, but such an investigation was outside the scope of our revised task description.

We modeled a Möbius ladder of two spins with antiferromagnetic coupling as an initial validation of our approximations, as the ground state for these systems can be well understood. Furthermore, as the number, N, of spins in the ladder increases, they continue to bifurcate in a similar manner. Figure 9 illustrates these effects. In each case we increase the pump strength from values below the lasing threshold to values above this threshold. Simulated homodyne measurements record the spins as a real (amplitude) quadrature component of each OPO, representing an individual spin state. This was done for both the Gaussian and Stochastic ODE approximation models. Both models exhibited bifurcations as the pump strength is increased. The Gaussian models tended to be smoother and delayed, occurring at higher pump strength than in the Stochastic ODE model. The latter more closely resembled the behavior observed in actual experiments of the CIM, as shown in Fig. 10, suggesting that the Stochastic Model, with its more faithful approximation to the physical dynamics, provides a better model of the CIM.

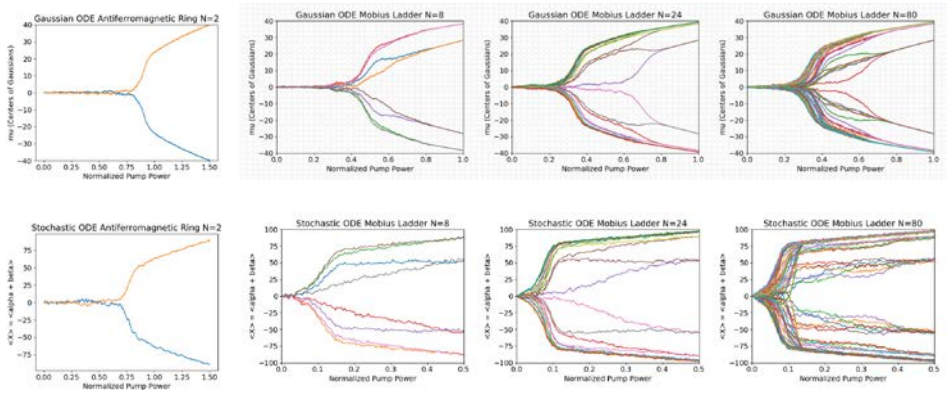

Figure 9: For Möbius ladder couplings, bifurcation of the simulated spins as the pump term increases. The spins still bifurcate even when modeling many (N=80) logical bits. The important consideration is whether the spins have settled into a ground state configuration.

To assess the impact of this higher fidelity model on performance, we ran each model on a Sherrington-Kirkpatrik spin glass problem, for which $h_i = 0$ and $J_{ij} = \pm 1$ represents all-to-all random coupling between spins. Figure 11 shows an example of these comparisons for an ensemble of spin-glass problems using either 90 or 110 maximally coupled spins. The plots show histograms of the final minimum energy over a number of independent runs. In general, the stochastic approximation gives a statistically smaller final energy, representing a better solution and one closer to the global minimum. This comports with our prior observation that a model that is more faithful the quantum physics of the problem leads to improved performance and suggests that there may be a quantum advantage imparted by this approach. The results of this aspect of the investigation were presented by Ms. Josey Hanish at the 21st annual Southwest Quantum Information (SQuInt) workshop on 10 February 2019 in Albuquerque, New Mexico.

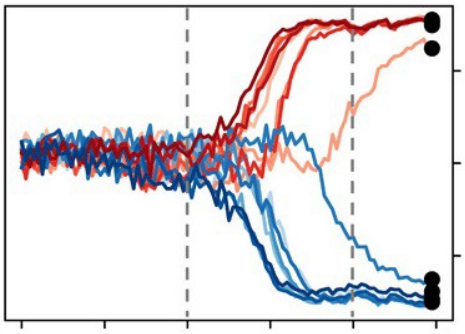

Figure 10: Experimentally observation bifurcation of OPOs in the CIM. (Figure from Ref. [1].)

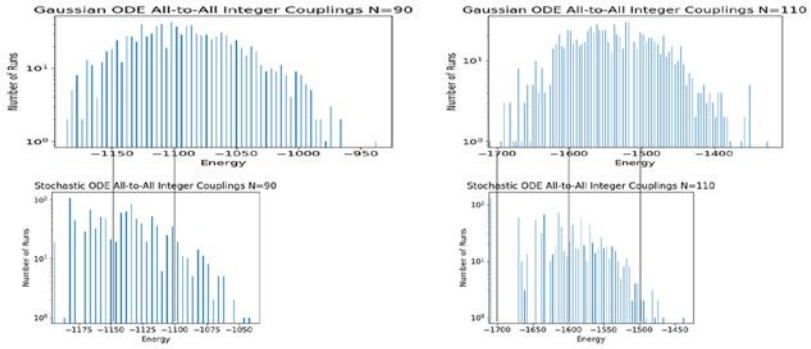

Figure 11: Comparison of performance for Gaussian and stochastic approximations of the CIM on spin-glass problems with 90 (left) and 110 (right) spins. The top and bottom plots are properly scaled for comparison.

4.2 MBQC

Using our decoder, we performed a series of analyses to determine if a threshold for fault tolerance could be found numerically for either the **X** or **Z** decoder. These results are described in greater detail in Ref. [25]. Fault tolerance is guaranteed by the Threshold theorem, provided the probability of an error is sufficiently low [26]. In particular, we considered the performance of each decoder as the error rate or probability of error, p, was varied and for difference code distances, d. We expect that when the probability of a physical errors is high that codes with a smaller code distance will perform better; i.e., there will be a lower probability of the decoder failing. This is due to the fact that larger code distances require a greater number of physical qubits for encoding and, hence, hold a greater potential for failure. As the error rate decreases, it is possible that larger codes may be capable of correcting more errors, due to the increased code distance, than arise due simply to the greater number of physical qubits that may experience an error. The error rate at which this happens is the threshold for fault tolerance. If such as threshold exists for a given decoding scheme, then a device that can be built with sufficiently low physical errors and in a scalable manner can, in theory, experience arbitrarily low failure rates.

We numerically tested both the **X** decoder and the **Z** decoder under an assumption of independent and identically distributed local noise. That is, each physical qubit would experience an error with the same probability p, and such an event is independent of any other qubit. For the **X** decoder, only **X** errors were considered, while for the **Z** decoder only **Z** errors were considered. For the Each data point was found using between 10^4 and 10^7 Monte Carlo simulations. The results are summarized in Figs. 12 and 13. There, error bars represent the standard deviation of the mean, given by $\sqrt{p_f(1-p_f)/N}$, where p_f is the decoding failure probability and N is the number of Monte Carlos simulations used.

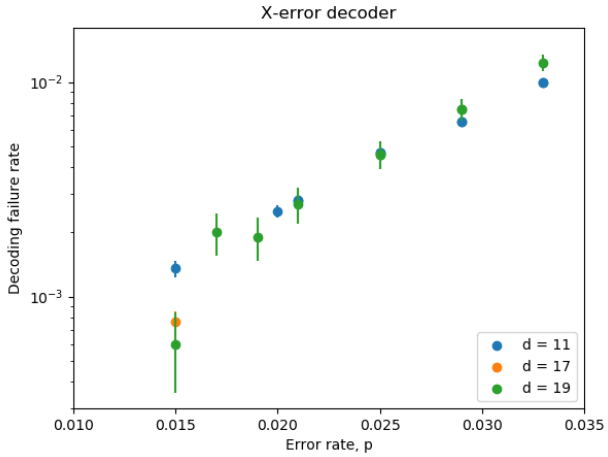

Figure 12: Performance of the X decoder under local noise.

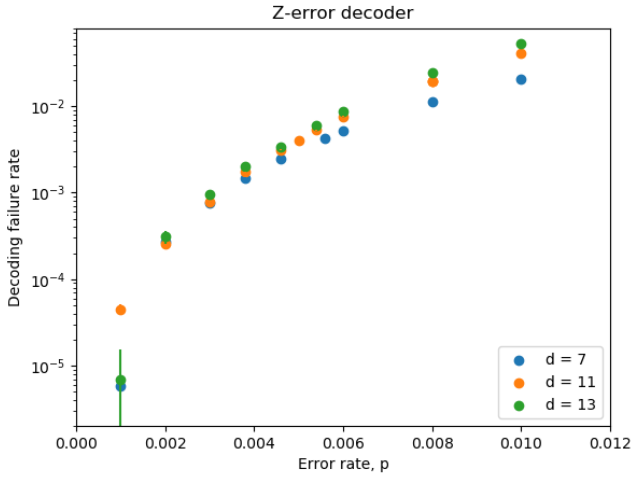

Figure 13: Performance of the Z decoder under local noise.

The data found from testing of the **X** decoder is shown in Fig. 12. As expected, we find that smaller code sizes outperform larger ones above $p = 3\%$, as indicated by a smaller decoding failure rate, while larger code sizes actually perform better than smaller ones below $p = 1.5\%$. In particular, for $p = 1.5\%$ we find the failure rates for a code size of $d = 11$ is about 1.5%, while that for codes sizes of $d = 17$ and $d = 19$ drop to about 0.65% and 0.40%, respectively. This is the signature of a fault tolerance threshold. However, because the error bars from numerical sampling overlap in between these points, we cannot pinpoint a precise threshold. We therefore conclude that there is strong evidence for a threshold for the **X** decoder that is between 1.5% and 3%.

The **Z** decoder data is shown in Fig. 13. Sub-threshold data, where larger codes outperform smaller codes, appears at or above $p = 0.1\%$. The different code sizes start to perform similarly near $p = 0.02\%$ and exhibit some crossover at $p = 0.01\%$. We therefore estimate the threshold for the **Z** decoder to be between 0.01% and 0.02%.

Although the decoders we have developed have been found to be quite successful in correcting independent **X** and **Z** errors on the lattice of the encoding physical qubits, such noise models, while commonly assumed in theoretical quantum error correction research, are not expected to provide an accurate characterization of the noise mechanisms in a realistic hardware implementation. We therefore recommend that future work address these shortcomings by considering more physically realistic noise models, assessing the performance of the current decoders, and improving the encoding and decoding schemes to recover fault tolerance under less ideal noise modeling assumptions.

5 Conclusions

5.1 CIM

We performed numerical simulations of the CIM under both the stochastic and Gaussian approximations using the benchmark problems and compared their performance to that of the NMFA algorithm. We found that the behavior of the stochastic approximation more closely resembled that of the physical CIM system and, therefore, seemed to capture more of the quantum effects needed for improved performance. This result suggests that any improvement in performance of the stochastic model might be explained by the fact that it captures more, but not all, of the quantum physics associated with the CIM.

In general, the stochastic approximation outperformed the Gaussian approximation, suggesting that a more fully quantum approach does yield better performance. However, the NMFA algorithm outperformed both of these, suggesting that classical heuristics can overcome this slight quantum advantage. This result shows promise for a full master equation solution of the CIM and suggests quantum effects are relevant to its performance. However, the current FPGA-based implementation of the CIM, however, does not appear to be capable of realizing this potential quantum advantage.

5.2 MBQC

The highest possible values for correction of **X** errors and **Z** errors in a 3D color code with periodic boundaries is 27.6% and 1.9% respectively [27]. Our decoder achieves thresholds an order of magnitude below this. Previous tests of the restriction decoder on the *bcc* lattice without boundaries found a threshold of 0.077% for the **Z** decoder and estimated (though not numerically tested) a threshold of 13.1% for the **X** decoder [10]. The **Z** decoder threshold of 0.046% found in [28] using a "clustering decoder," to our knowledge, is the only previous threshold found for a 3D color code with boundaries (though it was not tested on the *bcc* lattice). The role of boundaries is unclear; on one hand, we do not expect the thresholds for two codes which only differ in their boundaries to be much different, because for large code sizes almost all qubits lie in the bulk of the lattice. For the toric and the surface codes, this is true. However, for the family of 3-dimensional color codes where the number of physical qubits scales as d^3 it is difficult to test large enough code sizes that boundaries become unimportant. Indeed, 31.2% of qubits in the largest code we test, $d = 17$, lie on a boundary. It may be an interesting question to pursue how much an experimentally determined threshold depends on the size of the codes used in numerical simulation.

While our decoders do not perform as well as previous ones, we are able to adapt the restriction decoder to boundaries. The success of adapting the restriction decoder into a fault-tolerant protocol for the 2D color code [24] inspires hope that similar approaches may be used to improve performance of the tetrahedral color code. Tetrahedral color codes are the building blocks of a particularly elegant proposal for fault-tolerance called *colorful quantum computing*, which can be implemented using only transversal gates and a 2D lattice of physical qubits. Our work is a first step towards being able to numerically assess the performance of colorful quantum computing.

6 References

[1] R. Hamerly, T. Inagaki, P. McMahon, D. Venturelli, A. Marandi, and T. Onodera. Experimen- tal investigation of performance differences between coherent Ising machines and a quantum annealer. *Science Advances*, **5**:eaau0823, 2019.

[2] A. King, W. Bernoudy, J. King, A. Berkley, and T. Lanting. Emulating the coherent Ising machine with a mean-field algorithm. https://arxiv.org/abs/1806.08422, 2018.

[3] D. Browne and T. Rudolph. Resource-efficient linear optical quantum computation. *Physical Review Letters*, **95**:010501, 2005.

[4] M. Aramon, G. Rosenberg, E. Valiante, T. Miyazawa, H. Tamura, and H. Katzgraber. Physics- inspired optimization for quadratic unconstrained problems using a digital annealer. *Frontiers of Physics*, **7**:48, 2019.

[5] X. Qiang et al. Large-scale silicon quantum photonics implementing arbitrary two-qubit pro- cessing. *Nature Photonics*, **12**:534, 2018.

[6] N. Usher and D. Browne. Noise in one-dimensional measurement-based quantum computing.
Quantum Information and Computation, **17**:1372, 2017.

[7] T. Rudolph. Why I am optimistic about the silicon-photonic route to quantum computing.
APL Photonics, **2**:030901, 2017.

[8] M. Gimeno-Segovia, S. Shadbolt, D. Browne, and T. Rudolph. From three-photon Greenberger- Horne-Zeilinger states to ballistic universal quantum computation. *Physical Review Letters*, **115**:020502, 2015.

[9] H. Bombín. 2D quantum computation with 3D topological codes. https://arxiv.org/abs/1810.09571, 2018.

[10] A. Kubica and N. Delfosse. Efficient color code decoders in $d \geq 2$ dimensions from toric code decoders. https://arxiv.org/abs/1905.07393, 2019.

[11] B. Eastin and E. Knill. Restrictions on transversal encoded quantum gate sets. *Physical Review Letters*, **102**:110502, Mar 2009.

[12] H. Bombín. Transversal gates and error propagation in 3D topological codes. https://arxiv.org/abs/1810.09575, 2018.

[13] P. Webster and S. Bartlett. Fault-tolerant quantum gates with defects in topological stabiliser codes. https://arxiv.org/abs/1906.01045, 2019.

[14] R. Raussendorf and J. Harrington. Fault-tolerant quantum computation with high threshold in two dimensions. *Physical Review Letters*, **98**:190504, May 2007.

[15] R. Jozsa. An introduction to measurement based quantum computation. *NATO Science Se- ries, III: Computer and Systems Sciences. Quantum Information Processing-From Theory to Experiment*, **199**:137, 2006.

[16] E. Tiunov, A. Ulanov, and A. Lvovsky. Annealing by simulating the coherent Ising machine.
Optics Express, **27**:10288, 2019.

[17] F. Liersand M. Jünger. Spin Glass Server. https://informatik.uni-koeln.de/spinglass.

[18] A. Kubica and M. Beverland. Universal transversal gates with color codes: A simplified ap- proach. *Physical Review A*, **91**:032330, 2015.

[19] H. Bombín and M. Martin-Delgado. Topological computation without braiding. *Physical Review Letters*, **98**:160502, 2007.

[20] A. Kubica and J. Preskill. Cellular-automaton decoders with provable thresholds for topological codes. *Physical Review Letters*, **123**:020501, 2019.

[21] A. Aloshious and P. Sarvepalli. Decoding toric codes on three dimensional simplical complexes. https://arxiv.org/abs/1911.06056.

[22] A. Aloshious and P. Sarvepalli. Projecting three-dimensional color codes onto three-dimensional toric codes. *Physical Review A*, **98**:012302, Jul 2018.

[23] D. Wang, A. Fowler, A. Stephens, and L. Hollenberg. Threshold error rates for the toric and surface codes. https://arxiv.org/abs/0905.0531, 2009.

[24] C. Chamberland, A. Kubica, T. Yoder, and G. Zhu. Triangular color codes on trivalent graphs with flag qubits. https://arxiv.org/abs/1911.00355, 2019.

[25] S. Turner, J. Hanish, E. Blanchard, N. Davis, and B. La Cour. A decoder for the color code with boundaries. https://arxiv.org/abs/2003.11602, 2020.

[26] M. Nielsen and I. Chuang. *Quantum Computation and Quantum Information*. Cambridge University Press, 10th edition, 2010.

[27] A. Kubica, M. Beverland, F. Brandao, J. Preskill, and K. Svore. Three-dimensional color code thresholds via statistical-mechanical mapping. *Physical Review Letters*, **120**:180501, 2018.

[28] B. Brown, N. Nickerson, and D. Browne. Fault-tolerant error correction with the gauge color code. *Nature Communications*, **7**:12302, 2016.

7 List of Acronyms

AFRL — Air Force Research Laboratory

BCC — Body Centered Cubic

CIM — Coherent Ising Machine

D/A — Diagonal/Antidiagonal

FPGA — Field Programmable Gate Array

GHZ — Greenberger–Horne–Zeilinger

H/V — Horizontal/Vertical

HWP — Half-Wave Plate

MBQC — Measurement-Based Quantum Computing

MWPN — Minimum Weight Perfect Matching

NMFA — Noisy Mean Field Algorithm

ODE — Ordinary Differential Equation

OPO — Optical Parametric Oscillator

PBS — Polarizing Beamsplitter

PDC — Parametric Downconversion

PNR — Photon Number Resolving

QUBO — Quadratic Unconstrained Binary Optimization